AGU PUBLICATIONS

Geophysical Research Letters

RESEARCH LETTER
10.1002/2016GL071807

Key Points:
- EMIC waves are capable of scattering sub-MeV electrons into the bounce loss cone
- Only 11% of EMIC-related electron precipitation events studied were strongly relativistic (i.e., 1–4 MeV)
- We provide evidence to support recently published theoretical predictions of EMIC waves scattering nonresonant sub-MeV energy electrons

Supporting Information:
- Supporting Information S1

Correspondence to:
A. T. Hendry,
aaron.hendry@otago.ac.nz

Citation:
Hendry, A. T., C. J. Rodger, and M. A. Clilverd (2017), Evidence of sub-MeV EMIC-driven electron precipitation, *Geophys. Res. Lett.*, *44*, 1210–1218, doi:10.1002/2016GL071807.

Received 1 NOV 2016
Accepted 9 JAN 2017
Accepted article online 11 JAN 2017
Published online 9 FEB 2017

Evidence of sub-MeV EMIC-driven electron precipitation

Aaron T. Hendry[1], Craig J. Rodger[1], and Mark A. Clilverd[2]

[1]Department of Physics, University of Otago, Dunedin, New Zealand, [2]British Antarctic Survey (NERC), Cambridge, UK

Abstract Electromagnetic ion cyclotron (EMIC) waves are potentially important drivers of the loss of energetic electrons from the radiation belts. Numerous theoretical calculations exist with conflicting predictions of one of the key parameters: the minimum resonance energy of electrons precipitated into the atmosphere by EMIC waves. In this study we initially analyze an EMIC electron precipitation event using data from two different spacecraft instruments to investigate the energies involved. Combining observations from these satellites, we find that the electron precipitation has a peak flux at ~250 keV. Extending the analysis technique to a previously published database of similar scattering events, we find that the peak electron precipitation flux occurs predominantly around 300 keV, with only ~11% of events peaking in the 1–4 MeV range. Such a significant population of low-energy EMIC-driven electron precipitation events highlights the possibility for EMIC waves to be significant drivers of radiation belt electron losses.

1. Introduction

Electromagnetic ion cyclotron (EMIC) waves have long been identified as potential drivers of energetic ion [e.g., *Lyons and Thorne*, 1972] and relativistic electron [e.g., *Thorne and Kennel*, 1971] loss from the outer radiation belt. EMIC are Pc1–2 waves generated at the magnetic equator by thermal anisotropies in the ring current proton population [e.g., *Cornwall*, 1965], with enhanced occurrence following geomagnetic storms and substorms [*Fraser et al.*, 2010]. EMIC waves are observed across a wide range of L shells [e.g., *Meredith et al.*, 2014; *Usanova et al.*, 2012; *Min et al.*, 2012] and primarily in the noon-to-dusk magnetic local time (MLT) sector [e.g., *Anderson et al.*, 1992; *Halford et al.*, 2010; *Clausen et al.*, 2011; *Usanova et al.*, 2012], although recent results have suggested that wave generation may occur more uniformly in MLT [*Saikin et al.*, 2015; *Hendry et al.*, 2016]. EMIC waves are grouped into hydrogen, helium, and oxygen band waves based on their frequency, separated by the helium and oxygen gyrofrequencies, respectively.

The ability for EMIC waves to resonate with radiation belt electrons is strongly controlled by the frequency of the wave; as the wave frequency approaches the local ion gyrofrequency, the minimum resonant energy E_{min} rapidly drops [e.g., *Ukhorskiy et al.*, 2010; *Omura and Zhao*, 2013]. The limits of E_{min} have been widely studied theoretically. *Meredith et al.* [2003] used satellite-based EMIC wave observations and quasi-linear diffusion theory to suggest that, except in regions of high-plasma density, E_{min} was restricted to >2 MeV. Subsequent work has shown that for finite frequency width waves very close to the ion gyrofrequencies, E_{min} could drop as low as ~100 keV [*Ukhorskiy et al.*, 2010]; however, wave damping due to warm plasma effects at these frequencies may mean that the practical limit is closer to >1 MeV [*Chen et al.*, 2011].

Test particle simulations of EMIC electron resonance have also shown varied results. *Li et al.* [2007] showed that helium band waves could have minimum resonance energies as low as 400 keV in regions of high-plasma density, while *Jordanova et al.* [2008] suggested that EMIC resonance was limited to energies >1 MeV, again both using quasi-linear theory. However, recent simulations using nonlinear theory have shown resonance energies as low as 500 keV [*Omura and Zhao*, 2013].

In recent years nonresonant scattering by EMIC waves has also been suggested as a potential source of sub-MeV electron loss; in the recently published study by *Chen et al.* [2016], it was concluded that electron loss is possible for energies as low as a few hundred keV.

Experimental observations of EMIC-driven electron precipitation reported in the literature are surprisingly rare and until recently were largely limited to case studies. Calculations of precipitating electron energies from these studies has shown varied results. Modeling of subionospheric radio waves and riometer responses to EMIC-driven electron precipitation has shown minimum electron energies as low as 200–300 keV in some

cases [*Clilverd et al.*, 2015; *Rodger et al.*, 2015], yet as high as 2 MeV in others [*Rodger et al.*, 2008]. Balloon-based bremsstrahlung X-ray observations have shown conflicting minimum precipitation energies, with some as low as 400–500 keV [*Millan et al.*, 2002, 2007; *Woodger et al.*, 2015] and others in the >1 MeV range [*Lorentzen et al.*, 2000; *Li et al.*, 2014]. Results from the Van Allen Probes have suggested that EMIC wave-driven precipitation might be restricted to ultrarelativistic energies (2–8 MeV) [*Usanova et al.*, 2014].

Clearly, there is significant experimental evidence to suggest that EMIC-driven electron precipitation occurs over a wide range of energies, including sub-MeV energies. However, it is not possible to determine if these sub-MeV case studies are rare outliers or indicative of typical EMIC-driven precipitation energies. To investigate how likely this sub-MeV precipitation is, we must consider a large number of EMIC wave-driven precipitation events.

In this study we initially examine a single-electron precipitation event with a signature indicative of EMIC wave activity (section 3), using a combination of data from Polar-orbiting Operational Environmental Satellite Medium Energy Proton and Electron Detector (POES MEPED) instruments and the Demeter spacecraft. We show that detectors from either spacecraft can be used to determine the range of electron energies precipitated by EMIC-driven scattering (section 3.1). We then extend this analysis to a database of similar precipitation events, determining the range of electron precipitation energies observed (section 4).

2. Instrument Description

We have made use of three satellite-based instruments to investigate the energy spectra of the EMIC-scattered electron precipitation. These are outlined below.

2.1. POES MEPED

The main instrument used in this study is the Medium Energy Proton and Electron Detector (MEPED) carried by the Polar-orbiting Operational Environmental Satellite (POES) constellation. The MEPED instrument measures energetic electron and proton fluxes within the radiation belts using four directional particle telescopes, two each for electrons and protons, which ostensibly measure trapped and loss cone particles. The pitch angle populations being sampled by each telescopes are determined by the location of the satellite (see *Rodger et al.* [2010a, 2010b], for detailed descriptions of the populations that each telescope measures). Throughout this paper, we refer exclusively to the 0° loss cone telescopes, unless otherwise stated.

Each of the MEPED electron telescopes has three energy channels, measuring electron fluxes nominally in the >30 keV, >100 keV, and >300 keV energy ranges (called E1, E2, and E3, respectively). The proton telescopes have six energy channels, P1–P6, which sample from 30 keV up to >6900 keV. A detailed description of the POES satellite instruments can be found in *Evans and Greer* [2000].

The MEPED electron and proton telescopes are known to suffer from cross contamination, with >∼100 keV protons contaminating the electron detectors and >∼500 keV electrons contaminating the proton detectors. In particular, the P6 proton channel is strongly contaminated by relativistic electrons >∼800 keV. In the absence of high-energy protons, we are able to use this channel as a fourth electron detector. When using the P6 channel in this manner, we refer to it as the E4 channel to avoid confusion, following the example of *Peck et al.* [2015]. A full quantitative analysis of the POES MEPED cross-contamination issues can be found in *Yando et al.* [2011].

2.1.1. POES-Detected EMIC Event Database

In this study, we investigate a database of EMIC-driven electron precipitation events detected in POES MEPED data, using an algorithm described by *Carson et al.* [2013]. This algorithm identifies potential EMIC wave activity in POES MEPED data by searching for simultaneous bursts of relativistic electron and energetic proton precipitation in the E4 and P1 (30–80 keV proton) channels, respectively, a likely EMIC signature previously identified by several studies [e.g., *Miyoshi et al.*, 2008; *Sandanger et al.*, 2009] and confirmed by *Hendry et al.* [2016].

We use a database of 3777 precipitation triggers from 1998 to 2015 created by *Hendry et al.* [2016]. *Hendry et al.* [2016] showed that for precipitation triggers occurring directly overhead ground-based magnetometers, up to 90% of the database triggers coincided with EMIC wave observations. This result suggests a strong link between the database triggers and EMIC wave activity, allowing us to investigate the characteristics of the EMIC wave-driven precipitation.

2.2. Demeter

We also use data from the Demeter satellite, focusing on the Instrument for Detecting Particles (IDP), an electron spectrometer with particularly high-energy resolution. The IDP measures electron fluxes across 126 channels spanning 90 keV to 2.3 MeV (17.9 keV per channel) at 4 s resolution. For energies above 800 keV, there are significant uncertainties in the energy resolution of the instrument, so care must be taken when using these fluxes [*Sauvaud et al.*, 2006]. A full description of the instrument can be found in *Sauvaud et al.* [2006], while a discussion of the pitch angles sampled as well as the uncertainties in the IDP measured flux can be found in *Whittaker et al.* [2013]. We also use wave data from the Instrument Champ Electrique (ICE) electric field instrument, sampling at 39 Hz.

3. Case Study—18 November 2005

On 18 November 2005 at 13:00:31 UT the NOAA 17 satellite, located at $L = 5.1$ and 0.6 MLT, observed a sudden increase in electron flux across all three MEPED electron channels as well as the P6 electron-contaminated channel. At this time NOAA 17 was located south of Tasmania, as shown in Figure 1a. Nearly simultaneously, an increase in flux was observed in the P1 proton channel. No flux was observed in the high-energy proton channels, indicating that all of the P6-observed flux was due to electrons (i.e., in this case P6 = E4). The flux increase was short-lived in all channels, lasting only 8 s in the MEPED data and spanning ~0.2 L shells. No electron flux was noted before or after the flux increase, suggesting that all of the observed flux was due to a single source. The event, one of the *Carson et al.* [2013] POES triggers mentioned above, is consistent with the expected characteristics of EMIC-driven electron precipitation [*Hendry et al.*, 2016].

On the same day at 13:36:43 UT the IDP instrument on board the Demeter satellite, located at $L = 5.2$ and 23.9 MLT, observed a sudden increase in electron flux. At the same time, the ICE instrument observed a burst of wave power between the hydrogen and helium gyrofrequencies, shown in Figure 1b, indicating the presence of EMIC waves. The spatial proximity of these observations to the POES event suggests that both satellites were observing the same event, slightly separated in time and space (see Figure 1a).

All of the IDP energy channels between 150 and 1500 keV showed significant enhancement above the background flux; for energies >1.5 MeV the flux approached the noise floor of the instrument. The background flux levels at the time of the enhancement were determined by linearly interpolating between the flux levels before and after the enhanced spectrum. The background (orange line) and enhanced flux (blue line) of the Demeter-observed event are both shown in Figure 1c. By taking the difference between this expected background and the event time flux we isolated the enhanced flux, as shown by the blue crosses in Figure 1d.

Although the Demeter IDP instrument samples ostensibly trapped flux with pitch angles just above the bounce loss cone, the strong diffusion of the electrons caused by EMIC waves [*Summers and Thorne*, 2003] means any electrons scattered into the bounce loss cone are likely to be present in the trapped detectors as well. When the Demeter flux at the event time was compared to the just trapped fluxes sampled by the POES MEPED 90°telescope, we found that the Demeter flux magnitudes and energy distribution closely resembled that seen in the POES trapped flux measurements and that both featured similar bursts of electron flux at the event time to the POES loss cone instrument (Table 1, discussed below). This suggests that all three detectors were sampling the same scattered electrons. A detailed comparison of the POES and Demeter-trapped fluxes, as well as further information on the ability of this wave to cause strong diffusion, is included in the supporting information to this article.

3.1. Event Analysis

The enhanced flux spectrum observed in the Demeter IDP instrument (Figure 1d) shows a rapid increase in flux starting between 150 and 250 keV, followed by a more gradual drop off in flux toward ~1500 keV. Previous studies have used power law [e.g., *Millan et al.*, 2002; *Rodger et al.*, 2015; *Clilverd et al.*, 2015] and *e*-folding [e.g., *Millan et al.*, 2007] distributions to describe the variation in the precipitation flux caused by EMIC wave-driven scattering. Some studies of EMIC-driven flux [e.g., *Li et al.*, 2013] have used "peaked" distributions to represent the electron flux distribution. Distributions of this last type are better able to produce a smooth increase in flux followed by a steady decrease in flux with energy, such as that seen in the Demeter data (Figure 1d). We use the following equations to represent these distributions:

$$j_{\text{power}}(E) = \begin{cases} 0 & E < E_{\text{min}} \\ AE^{\beta} & E \geq E_{\text{min}} \end{cases} \quad (1)$$

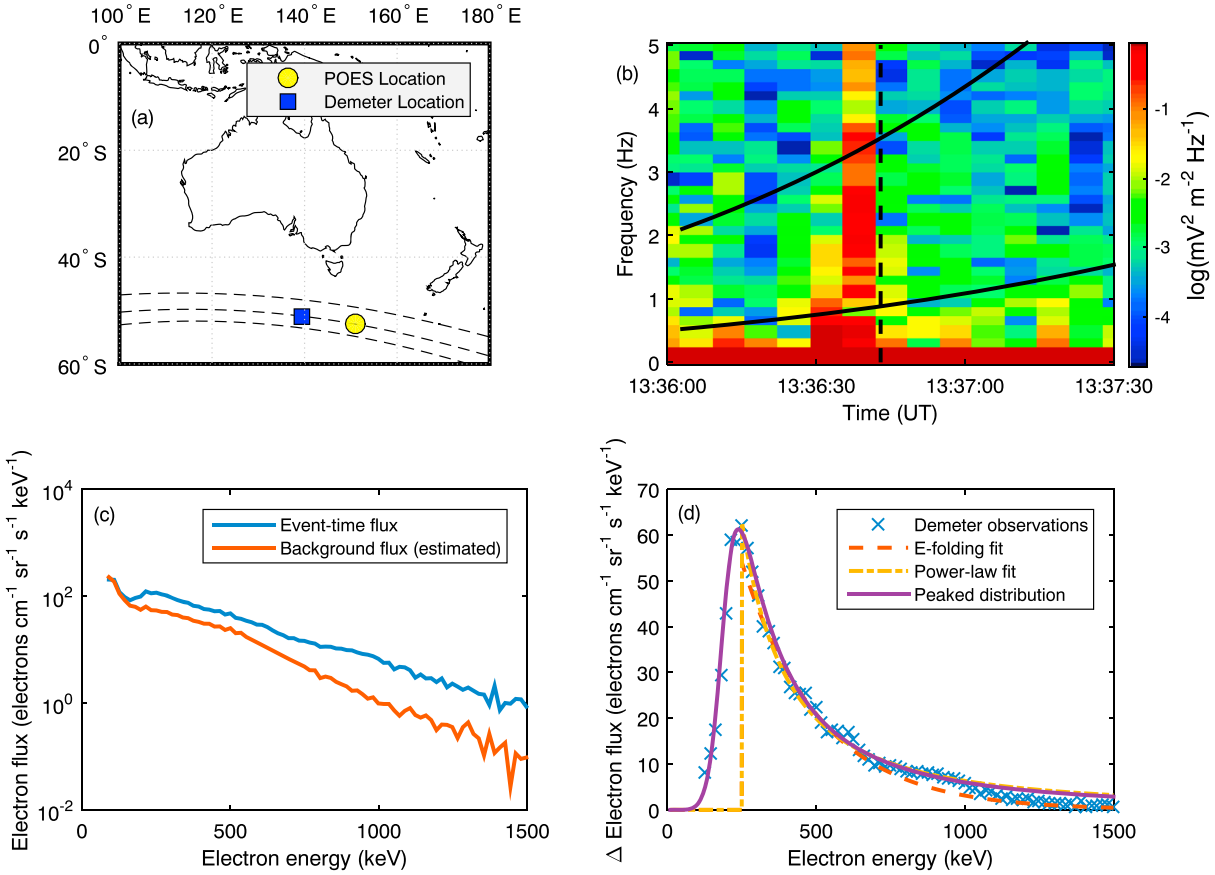

Figure 1. (a) Location of the POES and Demeter electron flux bursts observed on 18 November 2005, determined by tracing down the IGRF magnetic field line to an altitude of 110 km. L shells from 4 to 6 are superimposed on the map. (b) Demeter ICE E_z wave data, showing a burst of EMIC wave activity at the event time. The solid black lines indicate, from top to bottom, the hydrogen and helium gyrofrequencies determined at the IGRF magnetic equator. The dashed black line indicates the time of the electron flux burst in the Demeter IDP instrument. (c) Electron flux burst in the Demeter IDP instrument observed on 18 November 2005 at 13:36:43 UT, with estimated background flux. (d) Demeter IDP enhanced flux (i.e., with electron background removed) with fitted power law, *e*-folding, and peaked distributions.

$$j_{\text{efolding}}(E) = \begin{cases} 0 & E < E_{\text{min}} \\ Ae^{E/E_f} & E \geq E_{\text{min}} \end{cases} \tag{2}$$

$$j_{\text{peaked}}(E) = \left(e^{\alpha_1 - \beta_1 \ln E} + e^{-\alpha_2 + \beta_2 \ln E}\right)^{-1} \tag{3}$$

In the first two equations, A is a constant scaling value and E_{min} is the lower cutoff energy. For equation (1), β is the power law spectral index. For equation (2), E_f is the *e*-folding energy. Equation (3) produces a distribution peaked around a central energy E_p:

$$E_p = e^{\left(\alpha_1 - \ln\beta_1 + \alpha_2 + \ln\beta_2\right)/\left(\beta_1 + \beta_2\right)} \tag{4}$$

Table 1. The Calculated Response of the POES MEPED Instrument to Electron Flux Spectra Calculated According to Equations (1)–(3), Compared to the Measured POES MEPED Flux Response to an EMIC-Driven Electron Precipitation Event on 18 November 2005 at 13:00:31 UT[a]

		E-folding		Power law		"Peaked" distribution	
Channel	MEPED Reported	Calculated	Error	Calculated	Error	Calculated	Error
E1	62	59	4.8%	59	4.8%	62	0.0%
E2	56	56	0.0%	56	0.0%	56	0.0%
E3	30	36.5	22%	30	0.0%	28	6.7%
E4	11	3	73%	14	27%	11	0.0%

[a] All fluxes are in units of counts s^{-1}.

with the shape of the distribution controlled by the two spectral indices β_1 and β_2 and the scaling factors α_1 and α_2. Note that we are able to produce flux fits very similar to those seen in Figure 4b of *Li et al.* [2014] using the peaked distribution function described in equation (3).

Both equations (1) and (2) have a distinct lower cutoff energy, represented by E_{min}. The peaked distribution (equation (3)) does not have this same quantity, as the smooth increase in flux does not lend itself to a well defined lower limit. Instead, we refer to the central energy E_p, which represents where the peak flux intensity occurs and is a good indication of the energy around which the majority of the precipitation occurs.

The decaying portion (i.e., $E > 250$ keV) of the enhanced flux spectrum (Figure 1d) is well fit by both power law (equation (1); $\beta = -1.659$, $E_{min} = 250$ keV; $R^2 = 0.99$) and *e*-folding (equation (2); $E_f = -263$ keV, $E_{min} = 250$ keV; $R^2 = 0.98$) distributions, although the e-folding distribution appears to decay faster at higher energies than observed by Demeter. However, both of these distributions have sharp lower boundaries, which do not accurately reproduce the more gradual increase in flux seen from 150 to 250 keV in Figure 1d. In contrast, using the peaked distribution we are able to fit the Demeter flux with a more accurate spectrum ($\alpha_1 = 14.1, \alpha_2 = 31.5, \beta_1 = 1.8, \beta_2 = 6.8; E_p = 251$ keV; $R^2 = 0.99$). This spectrum, as well as the power law and *e*-folding spectra, are shown plotted over the enhanced Demeter flux data in Figure 1d.

Using these fitted distributions as approximations to the true flux spectrum, it is possible to produce a simulated POES response via the *Yando et al.* [2011] geometric factor curves combined with the algorithm described in *Green* [2013]. The results of this process are shown in Table 1. From these results it is evident that the peaked distributions accurately reproduces the POES-observed flux, with slightly less accurate results produced by the power law distribution. The *e*-folding distribution is unable to reproduce the E4 observed flux due to the more rapid drop off observed at higher energies.

4. Database Analysis

The previous section showed that it is possible to fit a POES-observed precipitation spectrum with a peaked distribution and suggests that EMIC-driven electron precipitation is possible down to energies of hundreds of keV. To investigate the range of energies in EMIC-driven electron precipitation events, the database of POES precipitation triggers described in section 2.1.1 is examined in a similar way to the case study.

4.1. The E3:E4 Ratio

It is possible to determine the approximate range of electron energies in a POES precipitation event by considering the relative flux magnitudes of the E3 and E4 channels at the time of the trigger. Considering the energy-dependent electron geometric factor curves for these channels [*Yando et al.*, 2011, Figures 4c and 5c], there is a crossover point in the sensitivities of the E3 and E4 channels at ~1400 keV. Thus, for electron flux at energies >1400 keV the E4 channel responds more strongly than E3, while for flux at energies <1400 keV the E3 channel responds more strongly.

Using this observation, we can posit that if the E4 channel reports less flux than the E3 channel (i.e., E3 > E4), the majority of the observed electron flux must have energies <1400 keV. If E3 < E4, however, we must have a strongly relativistic distribution, with the majority of the electron flux having energies >1400 keV. If we apply this test to the POES trigger database, we find that only 854/3777 triggers (~23%) have E3 < E4 and are thus strongly relativistic precipitation events.

4.2. Electron Precipitation Spectra

It is possible to make a more accurate estimate of the energy distribution of the EMIC-driven electron precipitation by fitting electron energy spectra to the POES MEPED data. In section 3.1 this was done using the Demeter-observed flux as an indicator of the true flux spectrum; for the vast majority of the events in the POES trigger database, no such Demeter data exists, making this approach impossible. Instead, for each POES trigger event we produce a test spectrum, calculate the POES instrument response to the spectra using the *Yando et al.* [2011] POES response curves, and iteratively generate spectra such that the error in the calculated response is minimized. In section 3.1 we found the peaked spectrum (equation (3)) produced the most accurate fit to the observed data. By fitting peaked distributions to all events in the trigger database, we can determine the approximate distribution of E_p for the POES-observed precipitation events.

It should be noted that given the small number of data points available from the POES instruments, in general, there will not exist a unique solution to the spectra-fitting problem. However, in the case of the peaked

distribution in equation (3), the peak energy E_p is fairly tightly constrained by the relative flux levels in each channel, in spite of the variation in the individual fitting parameters in the distribution.

4.2.1. Event Selection

To ensure an accurate fit of our test spectra to the POES precipitation data, we attempted to minimize any outside sources that might contaminate the data. The most significant of these contaminating factors was other radiation belt precipitation sources, in particular, substorms. Substorms are known to occur in similar MLT ranges to that of our event database and can cause significant electron precipitation across a wide range of energies and L shells [*Cresswell-Moorcock et al.*, 2013, and references therein]. Comparatively, the events in the trigger database are very narrow in L, typically $\Delta L < 0.2$. Consequently, we excluded substorm-contaminated events by removing triggers with significant background electron precipitation, i.e., those for which the flux before and after the main precipitation spike is significantly above the noise floor of the instrument. Chorus wave-induced precipitation is another potential source of contaminating electrons; however, chorus-induced precipitation would not trigger the *Carson et al.* [2013] algorithm as it does not generate a coincident proton precipitation spike and is typically a postmidnight MLT phenomenon [e.g., *Li et al.*, 2009]. As our database occurs predominantly premidnight, we expect little contamination from chorus wave activity.

We also excluded any events with any channel reporting <10 counts/s, as the uncertainty involved with fitting events so close to the noise floor was too great. We also considered the contamination of the POES electron channels by energetic (i.e., >100 keV) protons. If this contamination occurred during a POES trigger event, it could reduce the accuracy of any fitted electron spectra. Finally, we require the fit to be of good quality, as described below.

In total 1626/3777 events were removed due to low flux levels. Of the remaining 2151 events, 1489 were removed due to significant background flux in any of the electron channels. This left a total of 662 events for us to analyze (18% of the original database).

For each of the remaining 662 events, we ensured that we were fitting only electron data by removing the proton contamination (if any) from each of the electron channels. This was necessary for 265 events. To remove this contamination, we first determined the best fit for the proton flux data using a double Maxwellian distribution. This distribution was shown by *Peck et al.* [2015] to produce the best fit for POES MEPED proton fluxes, as validated against the higher-resolution Demeter IDP instrument. We then calculated the electron contamination produced by this proton distribution using the contamination geometric factors from *Yando et al.* [2011]. This left us with a "cleaned" event to which we fitted an electron flux spectrum using the method described above.

Figure 2a shows the occurrence distribution of the peak energy E_p of each of the fitted spectra, while Figure 2c shows the distribution of the maximum error for each event. We define the maximum error as the largest percentage difference of the calculated response from the measured response across all of the POES channels. For a small number of these events (52/662, ~8%) the maximum error was greater than 15%; these events have been excluded from further analysis, leaving 610 events. We note that ~66% of the events had a maximum error of <5%, indicating a very good fit.

The dominant population (~53%) of our fitted events have E_p values around 200–500 keV, with a secondary maximum (~17% of fitted events) occurring in the 0.8–4 MeV range. Very few events had $E_p > 4$ MeV (~1%). In section 4.1 we calculated a rough estimate of where the peak energy for a given event should occur using the ratio of the E3 and E4 channels. Repeating this for our fitted events, we find that ~14% of events have E3 < E4, and are thus strongly relativistic. Comparing the ratio to our calculated E_p, we find that roughly 89% of the events have $E_p < 1400$ keV, with 83% having $E_p < 1000$ keV, which is consistent with our rough estimate using the E3:E4 ratio.

4.2.2. Events With Wave Observations

Using the same precipitation event data set, *Hendry et al.* [2016] observed a large number of EMIC waves in ground-based magnetometers associated with the electron precipitation triggers. Of the 610 successfully fitted events described above, 228 were considered by *Hendry et al.* [2016], who looked for possible EMIC waves associated with the precipitation triggers. Of these 228, 123 (54%) were associated with observed EMIC waves. Figure 2b shows the distribution of E_p for these events, which is clearly very similar to that seen in Figure 2a. The most common values of E_p occur at the same energies for the much larger fitted set shown in Figure 2a. From this we have additional confidence that the E_p distribution seen in Figure 2a is indeed representative of typical EMIC-driven precipitation events.

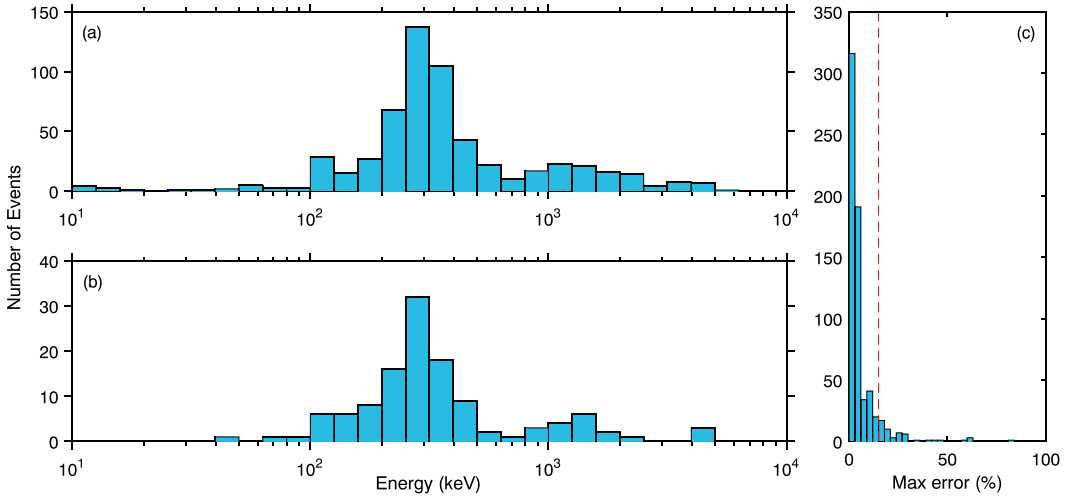

Figure 2. (a) The distribution of peak energies E_p among the fitted electron precipitation events. (b) The distribution of peak energies E_p for those events in Figure 2a that were directly linked to observed EMIC waves by *Hendry et al.* [2016]. (c) The maximum percentage error of any channel for each fitted event in Figure 2a. The red dotted line indicates the cutoff error of 15%, above which the events were considered "ill-fit."

For the 123 waves with triggers, 94% occurred in the helium or oxygen band, similar proportions to the *Hendry et al.* [2016] results. Too few waves were observed in the hydrogen band to discern any difference between the most common E_p values of these events and those in the helium or oxygen band.

5. Summary and Conclusions

In our case study we analyzed a burst of relativistic electron precipitation in the POES MEPED and Demeter IDP flux data that occurred around 13 UT on 18 November 2005 and which matched the signature of an EMIC wave electron precipitation event suggested by *Sandanger et al.* [2009]. This precipitation burst was accompanied by a burst of EMIC wave power observed in the Demeter ICE instrument. We have shown that both the Demeter spectrum and the POES MEPED precipitation fluxes were well fit by a peaked energy distribution, with the peak energy occurring at ~240 keV. This peak energy is at the lower limit of possible resonant energies indicated by theory and simulations [e.g., *Summers and Thorne*, 2003; *Li et al.*, 2007; *Omura and Zhao*, 2013; *Ukhorskiy et al.*, 2010] but consisted of the energies expected from nonresonant electron scattering by EMIC waves [*Chen et al.*, 2016].

We then examined a database of 3777 POES-detected EMIC precipitation events produced by *Hendry et al.* [2016]. We selected a subset of this database, excluding very small events and events with excessive background flux, leaving 662/3777 events. We removed the effects of proton contamination from these events before fitting the electron data with the same peaked energy distribution used in the case study. We found that the majority of the precipitation events (83%) had $E_p < 1$ MeV, with a smaller fraction (17%) showing E_p in the 0.8–4 MeV range, while only 1% had $E_p > 4$ MeV.

We compared our fitted events with the list of events associated with EMIC wave observations made by *Hendry et al.* [2016] using the same database. We found that the E_p distribution of fitted events (Figure 2b) that were associated with an EMIC wave observation was very similar to the E_p distribution for the entire set of fitted events (Figure 2a). This supports the idea that the E_p distributions reported here are representative of those distributions for EMIC-driven scattering.

Our results suggest that not only is sub-MeV EMIC-driven electron precipitation possible but that it is the dominant occurrence. This dominance may be a result of selection bias, due to both the greater populations of radiation belt electrons at these energies. The sub-MeV precipitation observed in this study is consistent with recent results showing EMIC waves causing nonresonant scattering of electrons with energies down to a few hundred keV [*Chen et al.*, 2016], though without further investigation into the driving mechanism, we cannot discard the possibility of a secondary, unknown precipitation driver causing this low-energy precipitation.

Acknowledgments
The research leading to these results has received funding from the European Community's Seventh Framework Programme (FP7/2007-2013) under grant agreement 263218. The authors wish to thank the personnel who developed, maintain, and operate the NOAA/POES spacecraft and the Demeter satellite. The data used in this paper are available at NOAA's National Geophysical Data Center (NGDC-POES MEPED data), and the CNES/CESR Centre de Donnees pour la Physique des Plasmas (CDPP-Demeter IDP and ICE data).

References

Anderson, B. J., R. E. Erlandson, and L. J. Zanetti (1992), A statistical study of Pc 1–2 magnetic pulsations in the equatorial magnetosphere: 1. Equatorial occurrence distributions, *J. Geophys. Res.*, *97*(A3), 3075–3088, doi:10.1029/91JA02706.

Carson, B. R., C. J. Rodger, and M. A. Clilverd (2013), POES satellite observations of EMIC-wave driven relativistic electron precipitation during 1998–2010, *J. Geophys. Res. Space Physics*, *118*, 232–243, doi:10.1029/2012JA017998.

Chen, L., R. M. Thorne, and J. Bortnik (2011), The controlling effect of ion temperature on EMIC wave excitation and scattering, *Geophys. Res. Lett.*, *38*, L16109, doi:10.1029/2011GL048653.

Chen, L., R. M. Thorne, J. Bortnik, and X.-J. Zhang (2016), Nonresonant interactions of electromagnetic ion cyclotron waves with relativistic electrons, *J. Geophys. Res. Space Physics*, *121*, 9913–9925, doi:10.1002/2016JA022813.

Clausen, L. B. N., J. B. H. Baker, J. M. Ruohoniemi, and H. J. Singer (2011), EMIC waves observed at geosynchronous orbit during solar minimum: Statistics and excitation, *J. Geophys. Res.*, *116*, A10205, doi:10.1029/2011JA016823.

Clilverd, M. A., R. Duthie, R. Hardman, A. T. Hendry, C. J. Rodger, T. Raita, M. Engebretson, M. R. Lessard, D. Danskin, and D. K. Milling (2015), Electron precipitation from EMIC waves: A case study from 31 May 2013, *J. Geophys. Res. Space Physics*, *120*, 3618–3631, doi:10.1002/2015JA021090.

Cornwall, J. M. (1965), Cyclotron instabilities and electromagnetic emission in the ultra low frequency and very low frequency ranges, *J. Geophys. Res.*, *70*(1), 61–69, doi:10.1029/JZ070i001p00061.

Cresswell-Moorcock, K., C. J. Rodger, A. Kero, A. B. Collier, M. A. Clilverd, I. Häggström, and T. Pitkänen (2013), A reexamination of latitudinal limits of substorm-produced energetic electron precipitation, *J. Geophys. Res. Space Physics*, *118*, 6694–6705, doi:10.1002/jgra.50598.

Evans, D. S., and M. S. Greer (2000), *Polar Orbiting Environmental Satellite Space Environment Monitor-2: Instrument Description and Archive Data Documentation*, US Dept. of Commerce, Natl. Oceanic and Atmos. Administr., Oceanic and Atmos. Res. Lab., Space Environ. Center, Boulder, Colo.

Fraser, B. J., R. S. Grew, S. K. Morley, J. C. Green, H. J. Singer, T. M. Loto'aniu, and M. F. Thomsen (2010), Storm time observations of electromagnetic ion cyclotron waves at geosynchronous orbit: GOES results, *J. Geophys. Res.*, *115*, A05208, doi:10.1029/2009JA014516.

Green, J. (2013), MEPED telescope data processing algorithm theoretical basis document, *Tech. Rep.*, NOAA NESDIS-NGDC. [Available at https://www.ngdc.noaa.gov/stp/satellite/poes/docs/NGDC/MEPED%20telescope%20processing%20ATBD_V1.pdf.]

Halford, A. J., B. J. Fraser, and S. K. Morley (2010), EMIC wave activity during geomagnetic storm and nonstorm periods: CRRES results, *J. Geophys. Res.*, *115*, A12248, doi:10.1029/2010JA015716.

Hendry, A. T., C. J. Rodger, M. A. Clilverd, M. J. Engebretson, I. R. Mann, M. R. Lessard, T. Raita, and D. K. Milling (2016), Confirmation of EMIC wave driven relativistic electron precipitation, *J. Geophys. Res. Space Physics*, *121*, 5366–5383, doi:10.1002/2015JA022224.

Jordanova, V. K., J. Albert, and Y. Miyoshi (2008), Relativistic electron precipitation by EMIC waves from self-consistent global simulations, *J. Geophys. Res.*, *113*, A00A10, doi:10.1029/2008JA013239.

Li, W., Y. Y. Shprits, and R. M. Thorne (2007), Dynamic evolution of energetic outer zone electrons due to wave-particle interactions during storms, *J. Geophys. Res.*, *112*, doi:10.1029/2007JA012368.

Li, W., R. M. Thorne, V. Angelopoulos, J. Bortnik, C. M. Cully, B. Ni, O. LeContel, A. Roux, U. Auster, and W. Magnes (2009), Global distribution of whistler-mode chorus waves observed on the THEMIS spacecraft, *Geophys. Res. Lett.*, *36*(9), L09104, doi:10.1029/2009GL037595.

Li, Z., R. M. Millan, and M. K. Hudson (2013), Simulation of the energy distribution of relativistic electron precipitation caused by quasi-linear interactions with EMIC waves, *J. Geophys. Res. Space Physics*, *118*, 7576–7583, doi:10.1002/2013JA019163.

Li, Z., et al. (2014), Investigation of EMIC wave scattering as the cause for the BARREL 17 January 2013 relativistic electron precipitation event: A quantitative comparison of simulation with observations, *Geophys. Res. Lett.*, *41*, 8722–8729, doi:10.1002/2014GL062273.

Lorentzen, K. R., M. P. McCarthy, G. K. Parks, J. E. Foat, R. M. Millan, D. M. Smith, R. P. Lin, and J. P. Treilhou (2000), Precipitation of relativistic electrons by interaction with electromagnetic ion cyclotron waves, *J. Geophys. Res.*, *105*(A3), 5381–5389, doi:10.1029/1999JA000283.

Lyons, L. R., and R. M. Thorne (1972), Parasitic pitch angle diffusion of radiation belt particles by ion cyclotron waves, *J. Geophys. Res.*, *77*(28), 5608–5616, doi:10.1029/JA077i028p05608.

Meredith, N. P., R. M. Thorne, R. B. Horne, D. Summers, B. J. Fraser, and R. R. Anderson (2003), Statistical analysis of relativistic electron energies for cyclotron resonance with EMIC waves observed on CRRES, *J. Geophys. Res.*, *108*(A6), 1250, doi:10.1029/2002JA009700.

Meredith, N. P., R. B. Horne, T. Kersten, B. J. Fraser, and R. S. Grew (2014), Global morphology and spectral properties of EMIC waves derived from CRRES observations, *J. Geophys. Res. Space Physics*, *119*, 5328–5342, doi:10.1002/2014JA020064.

Millan, R. M., R. P. Lin, D. M. Smith, K. R. Lorentzen, and M. P. McCarthy (2002), X-ray observations of MeV electron precipitation with a balloon-borne germanium spectrometer, *Geophys. Res. Lett.*, *29*(24), 4212, doi:10.1029/2002GL015922.

Millan, R. M., R. P. Lin, D. M. Smith, and M. P. McCarthy (2007), Observation of relativistic electron precipitation during a rapid decrease of trapped relativistic electron flux, *Geophys. Res. Lett.*, *34*, L10101, doi:10.1029/2006GL028653.

Min, K., J. Lee, K. Keika, and W. Li (2012), Global distribution of EMIC waves derived from THEMIS observations, *J. Geophys. Res.*, *117*, A05219, doi:10.1029/2012JA017515.

Miyoshi, Y., K. Sakaguchi, K. Shiokawa, D. Evans, J. Albert, M. Connors, and V. Jordanova (2008), Precipitation of radiation belt electrons by EMIC waves, observed from ground and space, *Geophys. Res. Lett.*, *35*, L23101, doi:10.1029/2008GL035727.

Omura, Y., and Q. Zhao (2013), Relativistic electron microbursts due to nonlinear pitch angle scattering by EMIC triggered emissions, *J. Geophys. Res. Space Physics*, *118*, 5008–5020, doi:10.1002/jgra.50477.

Peck, E. D., C. E. Randall, J. C. Green, J. V. Rodriguez, and C. J. Rodger (2015), POES MEPED differential flux retrievals and electron channel contamination correction, *J. Geophys. Res. Space Physics*, *120*, 4596–4612, doi:10.1002/2014JA020817.

Rodger, C. J., T. Raita, M. A. Clilverd, A. Seppälä, S. Dietrich, N. R. Thomson, and T. Ulich (2008), Observations of relativistic electron precipitation from the radiation belts driven by EMIC waves, *Geophys. Res. Lett.*, *35*, L16106, doi:10.1029/2008GL034804.

Rodger, C. J., M. A. Clilverd, J. C. Green, and M. M. Lam (2010a), Use of POES SEM-2 observations to examine radiation belt dynamics and energetic electron precipitation into the atmosphere, *J. Geophys. Res.*, *115*, A04202, doi:10.1029/2008JA014023.

Rodger, C. J., B. R. Carson, S. A. Cummer, R. J. Gamble, M. A. Clilverd, J. C. Green, J.-A. Sauvaud, M. Parrot, and J.-J. Berthelier (2010b), Contrasting the efficiency of radiation belt losses caused by ducted and nonducted whistler-mode waves from ground-based transmitters, *J. Geophys. Res.*, *115*, A12208, doi:10.1029/2010JA015880.

Rodger, C. J., A. T. Hendry, M. A. Clilverd, C. A. Kletzing, J. B. Brundell, and G. D. Reeves (2015), High-resolution in situ observations of electron precipitation-causing EMIC waves, *Geophys. Res. Lett.*, *42*, 9633–9641, doi:10.1002/2015GL066581.

Saikin, A. A., J.-C. Zhang, R. Allen, C. W. Smith, L. M. Kistler, H. E. Spence, R. B. Torbert, C. A. Kletzing, and V. K. Jordanova (2015), The occurrence and wave properties of H^+-, He^+-, and O^+-band EMIC waves observed by the Van Allen Probes, *J. Geophys. Res. Space Physics*, *120*, 7477–7492, doi:10.1002/2015JA021358.

Sandanger, M., F. Søraas, M. Sørbø, K. Aarsnes, K. Oksavik, and D. Evans (2009), Relativistic electron losses related to EMIC waves during CIR and CME storms, *J. Atmos. Sol. Terr. Phys.*, *71*(10-11), 1126–1144, doi:10.1016/j.jastp.2008.07.006.

Sauvaud, J., T. Moreau, R. Maggiolo, J.-P. Treilhou, C. Jacquey, A. Cros, J. Coutelier, J. Rouzaud, E. Penou, and M. Gangloff (2006), High-energy electron detection onboard DEMETER: The IDP spectrometer, description and first results on the inner belt, *Planet. Space Sci.*, *54*(5), 502–511, doi:10.1016/j.pss.2005.10.019, first Results of the DEMETER Micro-Satellite.

Summers, D., and R. M. Thorne (2003), Relativistic electron pitch angle scattering by electromagnetic ion cyclotron waves during geomagnetic storms, *J. Geophys. Res.*, *108*(A4), 1143, doi:10.1029/2002JA009489.

Thorne, R. M., and C. F. Kennel (1971), Relativistic electron precipitation during magnetic storm main phase, *J. Geophys. Res.*, *76*(19), 4446–4453.

Ukhorskiy, A. Y., Y. Y. Shprits, B. J. Anderson, K. Takahashi, and R. M. Thorne (2010), Rapid scattering of radiation belt electrons by storm-time EMIC waves, *Geophys. Res. Lett.*, *37*, L09101, doi:10.1029/2010GL042906.

Usanova, M. E., I. R. Mann, J. Bortnik, L. Shao, and V. Angelopoulos (2012), THEMIS observations of electromagnetic ion cyclotron wave occurrence: Dependence on AE, SYM-H, and solar wind dynamic pressure, *J. Geophys. Res.*, *117*, A10218, doi:10.1029/2012JA018049.

Usanova, M. E., et al. (2014), Effect of EMIC waves on relativistic and ultrarelativistic electron populations: Ground-based and Van Allen Probes observations, *Geophys. Res. Lett.*, *41*, 1375–1381, doi:10.1002/2013GL059024.

Whittaker, I. C., R. J. Gamble, C. J. Rodger, M. A. Clilverd, and J.-A. Sauvaud (2013), Determining the spectra of radiation belt electron losses: Fitting DEMETER electron flux observations for typical and storm times, *J. Geophys. Res. Space Physics*, *118*, 7611–7623, doi:10.1002/2013JA019228.

Woodger, L. A., A. J. Halford, R. M. Millan, M. P. McCarthy, D. M. Smith, G. S. Bowers, J. G. Sample, B. R. Anderson, and X. Liang (2015), A summary of the BARREL campaigns: Technique for studying electron precipitation, *J. Geophys. Res. Space Physics*, *120*, 4922–4935, doi:10.1002/2014JA020874.

Yando, K., R. M. Millan, J. C. Green, and D. S. Evans (2011), A Monte Carlo simulation of the NOAA POES medium energy proton and electron detector instrument, *J. Geophys. Res.*, *116*, A10231, doi:10.1029/2011JA016671.